The Astrophysical Journal, 739:27 (15pp), 2011 September 20 doi:10.1088/0004-637X/739/1/27

STAR FORMATION IN 30 DORADUS*

Guido De Marchi[1], Francesco Paresce[2], Nino Panagia[3,4,5], Giacomo Beccari[6], Loredana Spezzi[1], Marco Sirianni[1], Morten Andersen[1], Max Mutchler[3], Bruce Balick[7], Michael A. Dopita[8,9,10], Jay A. Frogel[11,25], Bradley C. Whitmore[3], Howard Bond[3], Daniela Calzetti[12], C. Marcella Carollo[13], Michael J. Disney[14], Donald N. B. Hall[10], Jon A. Holtzman[15], Randy A. Kimble[16], Patrick J. McCarthy[17], Robert W. O'Connell[18], Abhijit Saha[19], Joseph I. Silk[20], John T. Trauger[21], Alistair R. Walker[22], Rogier A. Windhorst[23], and Erick T. Young[24]

[1] European Space Agency, Space Science Department, Keplerlaan 1, 2200 AG Noordwijk, The Netherlands; gdemarchi@rssd.esa.int
[2] Istituto di Astrofisica Spaziale e Fisica Cosmica, Via Gobetti 101, 40129 Bologna, Italy
[3] Space Telescope Science Institute, 3700 San Martin Drive, Baltimore, MD 21218, USA
[4] INAF-CT, Osservatorio Astrofisico di Catania, Via S. Sofia 78, 95123 Catania, Italy
[5] Supernova Limited, OYV #131, Northsound Road, Virgin Gorda, British Virgin Islands
[6] European Southern Observatory, Karl-Schwarzschild-Str. 2, 85748 Garching, Germany
[7] Department of Astronomy, University of Washington, Seattle, WA 98195-1580, USA
[8] Mount Stromlo and Siding Spring Observatories, Research School of Astronomy & Astrophysics, Australian National University, Cotter Road, Weston Creek, ACT 2611, Australia
[9] Astronomy Department, King Abdulaziz University, P.O. Box 80203, Jeddah, Saudi Arabia
[10] Institute for Astronomy, University of Hawaii, 2680 Woodlawn Drive, Honolulu, HI 96822, USA
[11] Galaxies Unlimited, 8726 Hickory Bend Trail, Potomac, MD 20854, USA
[12] Department of Astronomy, University of Massachusetts, Amherst, MA 01003, USA
[13] Department of Physics, ETH-Zurich, Zurich 8093, Switzerland
[14] School of Physics and Astronomy, Cardiff University, Cardiff CF24 3AA, UK
[15] Department of Astronomy, New Mexico State University, Las Cruces, NM 88003, USA
[16] NASA-Goddard Space Flight Center, Greenbelt, MD 20771, USA
[17] Observatories of the Carnegie Institution of Washington, Pasadena, CA 91101-1292, USA
[18] Department of Astronomy, University of Virginia, Charlottesville, VA 22904-4325, USA
[19] National Optical Astronomy Observatories, Tucson, AZ 85726-6732, USA
[20] Department of Physics, University of Oxford, Oxford OX1 3PU, UK
[21] NASA-Jet Propulsion Laboratory, Pasadena, CA 91109, USA
[22] Cerro Tololo Inter-American Observatory, La Serena, Chile
[23] School of Earth and Space Exploration, Arizona State University, Tempe, AZ 85287-1404, USA
[24] SOFIA Science Center, NASA Ames Research Center, Moffett Field, CA 94035, USA
Received 2011 May 2; accepted 2011 June 13; published 2011 September 1

ABSTRACT

Using observations obtained with the Wide-Field Camera 3 on board the *Hubble Space Telescope*, we have studied the properties of the stellar populations in the central regions of 30 Dor in the Large Magellanic Cloud. The observations clearly reveal the presence of considerable differential extinction across the field. We characterize and quantify this effect using young massive main-sequence stars to derive a statistical reddening correction for most objects in the field. We then search for pre-main-sequence (PMS) stars by looking for objects with a strong ($>4\sigma$) $H\alpha$ excess emission and find about 1150 of them over the entire field. Comparison of their location in the Hertzsprung–Russell diagram with theoretical PMS evolutionary tracks for the appropriate metallicity reveals that about one-third of these objects are younger than ∼4 Myr, compatible with the age of the massive stars in the central ionizing cluster R 136, whereas the rest have ages up to ∼30 Myr, with a median age of ∼12 Myr. This indicates that star formation has proceeded over an extended period of time, although we cannot discriminate between an extended episode and a series of short and frequent bursts that are not resolved in time. While the younger PMS population preferentially occupies the central regions of the cluster, older PMS objects are more uniformly distributed across the field and are remarkably few at the very center of the cluster. We attribute this latter effect to photo-evaporation of the older circumstellar disks caused by the massive ionizing members of R 136.

Key words: galaxies: star clusters: individual (30 Dor) – galaxies: stellar content – Magellanic Clouds – stars: formation – stars: pre-main sequence

Online-only material: color figures

1. INTRODUCTION

Many years of effort have been spent on trying to understand the structure and evolution of the super star cluster NGC 2070, at the center of the 30 Doradus nebula in the Large Magellanic Cloud (LMC), otherwise known as the Tarantula nebula, since its discovery as such by Lacaille in 1751. In this case, the prize is clearly worth the effort as this object may hold the key to answers to many fundamental questions regarding the physics of the formation of stars, stellar clusters, and galaxies and their role in the cosmos (e.g., Brandl 2005). Thanks also to this effort, we now know much about the brightest stars more massive than ∼2–3 $M_\odot$ that can be more easily detected and

* Based on observations with the NASA/ESA *Hubble Space Telescope*, obtained at the Space Telescope Science Institute, which is operated by AURA, Inc., under NASA contract NAS5-26555.
[25] Also at: Astronomy Department, King Abdulaziz University, P.O. Box 80203, Jeddah, Saudi Arabia.

resolved. In spite of the large distances (∼50 kpc) involved (Hunter et al. 1995a), these objects can be studied even in the very compact core of NGC 2070, referred to as R 136, which was first resolved unambiguously by the *Hubble Space Telescope* (*HST*) using the Faint Object Camera (Weigelt et al. 1991; De Marchi et al. 1993). But we still know very little about the other part of this population consisting of the fainter, low-mass main-sequence (MS) and pre-MS (PMS) stars and brown dwarfs. These might be present in even larger numbers if the tapered power-law initial mass function (IMF) proposed recently by De Marchi et al. (2010b) for young and very old clusters continues to the hydrogen burning limit and beyond. Their number and spatial distribution are critical for understanding the low-mass star formation process in a cluster of very massive stars and their role in determining the ultimate fate of the cluster itself.

The current observational situation regarding low-mass stars in NGC 2070 is contradictory. Although there is good evidence for a significant population of these stars, the precise nature of their spatial and mass distributions is not well understood. Sirianni et al. (2000), using *V*- and *I*-band *HST* observations, claim that the mass function (MF) flattens below $\sim 2\,M_{\odot}$, while Zinnecker et al. (2002) and more recently Andersen et al. (2009), using *HST* observations in the *H* band, find no such feature in their data down to their completeness limit around $1\,M_{\odot}$. So far, little can be said of what happens below this limit, mainly because these stars in NGC 2070 and its compact core R 136 are very difficult to detect and characterize accurately. First, because of their inherent faintness especially with respect to the high background due to the numerous much brighter stars in the field. Second, because they scatter widely across the color–magnitude diagram (CMD) making accurate subtraction of field stars and older cluster PMS stars and subdwarfs near the MS unreliable without useful separation criteria. Finally, the patchy extinction across the face of the nebula (e.g., Indebetouw et al. 2009) needs to be properly accounted for in order to accurately determine their true brightness.

For these reasons, using the Wide-Field Camera 3 (WFC3), the new panchromatic camera on *HST*, is, in principle, ideal for the task of establishing the main characteristics of the low-mass population in NGC 2070. With its high spatial resolution over a wide field encompassing most of the central part of the cluster and its unprecedented sensitivity in the near-UV and IR, the WFC3 allows us to tackle for the first time most of the problems summarized above with some hope of resolving them. In this paper, we present the first results of a deep survey of NGC 2070 obtained in 2009 October as part of the Early Release Science programme with the WFC3 camera. This project has as its ultimate objective that of determining as accurately as possible the properties of the low-mass IMF in this cluster, which could be a prototype of the much larger and distant unresolved super star clusters in starburst galaxies. In order for this type of study to become possible, we must first carefully identify and distinguish from one another stars of different ages, since several generations of objects are known to populate the 30 Dor region (e.g., Walborn & Blades 1997).

So far, studies of the star formation history of 30 Dor have been limited to the most massive stars, typically above $20\,M_{\odot}$, and hence to the past 10 Myr or so, because these works rely on spectroscopy of individual objects that cannot easily be obtained for less massive stars (e.g., Selman et al. 1999). Clearly, access to a wider mass range is crucial, so the goal of this paper is to understand how star formation has proceeded for much smaller objects, i.e., stars with masses as low as $\sim 0.5\,M_{\odot}$. Therefore, in this work we concentrate on a systematic search for low-mass stars in the PMS phase, which we can identify in a reliable way and which allow us to study how star formation has proceeded in this area over the past ∼30 Myr. Only then will it be possible to address the properties of the MF, which will be the subject of future work.

Table 1
List of Filter Names, Number of Exposures, and Total Exposure Times of the WFC3 Observations of 30 Dor

Filter Name	$N_{\rm exp}$	$t_{\rm tot}$
F336W	24	8659
F438W	16	5174
F555W	20	6892
F656N	8	10805
F814W	20	10700
F110W	9	1518
F160W	12	7816

Note. Total exposure times ($t_{\rm tot}$) are in seconds.

The structure of this paper is as follows. We describe the observations in Section 2, the reduction of the data in Section 3, and the photometric analysis in Section 4. The correction for extinction and the resultant-corrected CMDs are presented in Section 5. The Hertzsprung–Russell (H-R) diagram and its analysis with recent PMS models are the topic of discussion in Section 6, where we also discuss the preliminary physical implications of our results on the star formation history in these regions. A summary is provided in Section 7.

2. OBSERVATIONS

The observations discussed in this paper were obtained in 2009 October (20–27) with the WFC3 on board the *HST*. We refer the reader to Dressel et al. (2010) for information about the WFC3 instrument and its performances. Six broadband and one narrowband filters were used in these observations, as shown in Table 1, where the number of exposures and the total exposure times in each filter are also given. Note that an extensive dithering pattern was employed, combining both long and short exposures, in order to improve the sampling of the telescope's point-spread function (PSF), to minimize the effects of detector blemishes, to cover the gap between the two detectors in the field of view, and to recover the magnitudes of the brightest objects that would otherwise saturate in long exposures.

For illustration purposes, Figure 1 presents a four-color composite image of the observed field. The colors result from assigning different hues to each monochromatic image, as indicated in the figure caption. The bright compact star cluster in the upper right-hand side of the frame is R 136, the core of the massive NGC 2070 association. A cursory glance at Figure 1 already shows that the center of the cluster is dominated by bright blue stars, although a handful of bright red objects are seen to the east of it, suggesting the presence of an older generation of stars. This is consistent with the conclusions of Selman et al. (1999), who found at least three generations of massive stars, with the youngest and bluest members more centrally concentrated. We will return in more detail to the spatial distribution of these objects in Section 4.

3. DATA REDUCTION AND PHOTOMETRY

Throughout this paper we will concentrate on the observations in the optical wavelength range, and in particular on the F555W,

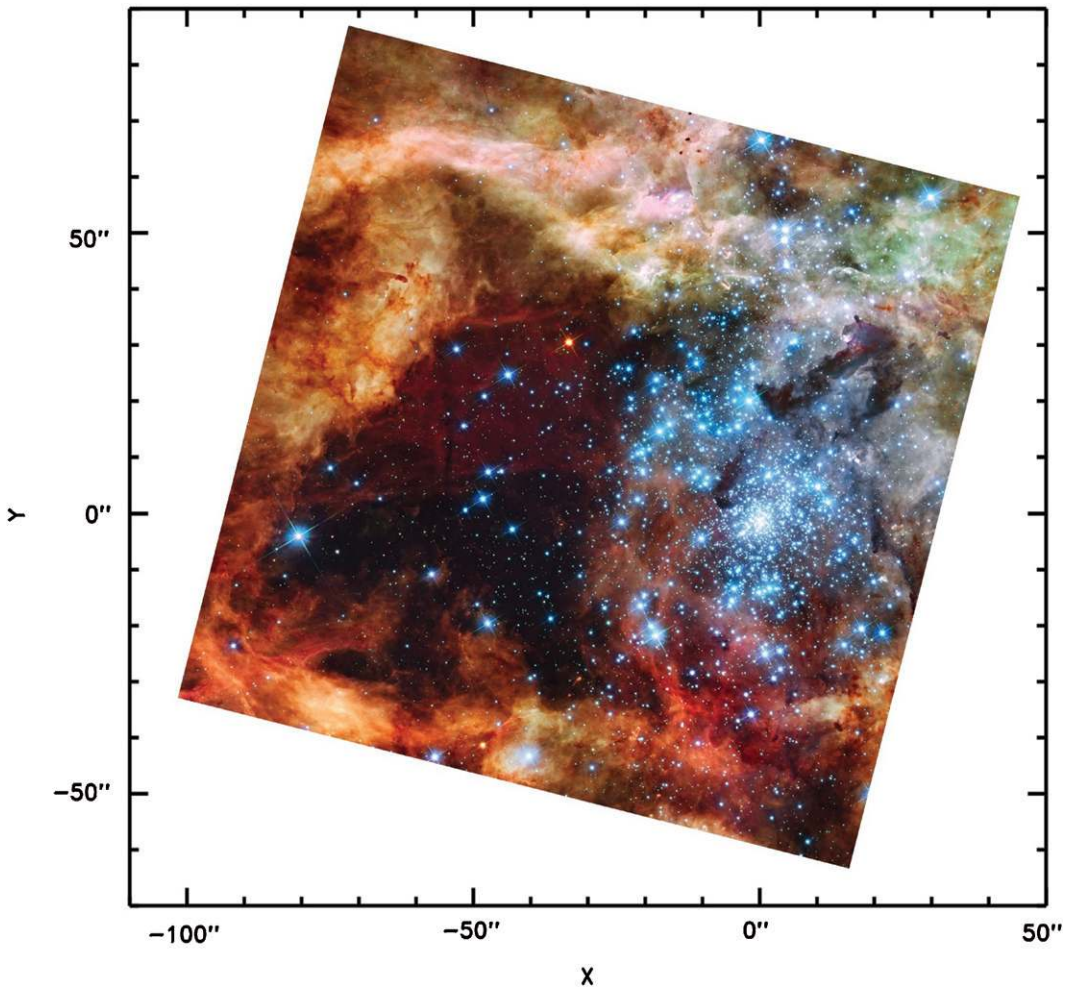

Figure 1. Color-composite image of the central part of the observed field. The blue channel is obtained by averaging the F336W and F439W filters, the F555W filter serves as green channel, the F814W filter as red channel, and the F656N filter is used as orange. The (0, 0) position in this figure corresponds to the nominal center of R 136 (RA = 05^{h} 38^{m} $43\overset{s}{.}3$, decl. = −69°06′08″; J2000) with north pointing up and east to the left. At the distance of R 136, 1 parsec corresponds to ∼4″. (This image was released by the Space Telescope Science Institute on 2009 December 15 as part of News Release number STScI-2009-32.)

(A color version of this figure is available in the online journal.)

F656N, and F814W bands (hereafter referred to as V, $H\alpha$, and I, respectively), whereas the entire WFC3 data set including the observations at IR wavelengths will be covered in more detail in a forthcoming paper (G. Beccari et al. 2011, in preparation).

As regards to the data reduction, the long and short exposures were treated in a different way. The deep data sets were combined using the IRAF *multidrizzle* task, with the appropriate calibration files and geometric distortion coefficients for the UVIS channel of the WFC3. Given the large number of deep frames available in the UVIS filters and the careful dithering strategy adopted for these observations, we were able to derive one single "drizzled" image per band, free of cosmic rays and blemishes and with a rather sharp and well-sampled PSF, ideal for the detection of faint stars. Producing a deep, high-quality combined image per filter is particularly useful in a field like 30 Dor where stars are embedded in extensive nebulosity associated with the gas that makes the photometry and the determination of the background more difficult on individual images.

Star detection and identification was performed by running the automated IRAF *daofind* routine separately on the V- and I-band drizzled frames, with the detection threshold set at 5σ above the local background level. In order for objects to be classified as real stars, we required that they be detected in both filters. The presence of numerous gas filaments and irregularities in the background can cause spurious detections, particularly in the $H\alpha$ band, where considerable emission is present (see Figure 1). For this reason, we visually inspected the detected stars and excluded from the bona fide list all the detections not clearly associated with point-like sources.

More specifically, we applied an unsharp-masking filter (e.g., Malin 1977), with a smoothing radius of 15 pixels meant to subtract the low-frequency signal. Unsharp masking makes structures and filaments in the nebular gas easier to see than in the direct image. In this way, we compared the structures and filaments with the positions of the detected stars, in order to avoid spurious detections (see Beccari et al. 2010 for an application of this method to the case of the massive Galactic cluster NGC 3603 observed with the same camera).

Once the master list was defined in this way, we proceeded to measure the magnitudes of each star with the IRAF *phot* aperture photometry task. Since the central regions are rather crowded, we opted for a photometric aperture of 3 pixel radius and a background annulus enclosing the area between 4 and 7 pixel radius around the stars. Following De Marchi et al. (1993), we took as background value the mode of the counts within the

annulus, in such a way to minimize the contamination due to neighboring objects. This procedure was not applied directly on the combined drizzled frames, but rather on a subset of those. More precisely, having at our disposal 16 deep exposures both in the V and I bands, we used multidrizzle to build for each filter four drizzled images, each comprising four individual exposures. We then ran the IRAF phot task on each of them, using as input coordinates the master list derived before. In this way, we could derive four independent measurements of the magnitude for each object in both the V and I bands and the standard deviation of the four measurements immediately provides the photometric uncertainty. We followed the same procedure in all other visible bands, including $H\alpha$ for which the four combined images comprise each two individual exposures.

The approach followed for the short exposures (ranging from a 0.5 s to 30 s in duration) is different, owing to the limited number of exposures available in each filter. In that case we performed photometry on each individual flat-fielded image using PSF fitting, having first built a proper PSF model on each frame using isolated and well-sampled stars, which was then fitted to each object in the images by means of the standard DAOPHOT/ALLSTAR routine. The reason why we did not use PSF-fitting photometry also for the deep exposures is that image combination with multidrizzle does not necessarily preserve the uniformity of the PSF.

The two photometric catalogs obtained in this way for the long and short exposures were independently calibrated following the specific recipes developed by Kalirai et al. (2009) for the UVIS channel of the WFC3. Briefly, all magnitudes were first rescaled to an aperture of 0.″4 and then transformed into the VEGAMAG system using the synthetic zero points given by Kalirai et al. (2009). The accuracy of the photometry in both catalogs is very good. The typical photometric uncertainty over the entire sample ranges from <0.02 mag at $V < 20$ or $I < 19$ to ∼0.2 mag at $V = 26.5$ or $I = 25.5$ (note that in the following sections we will limit our study to objects with the smallest uncertainties, as indicated).

Finally, the two photometric catalogs were combined and merged so as to avoid duplications. We used stars in the magnitude range $16 < V < 19$, where errors are small, to verify the integrity of the photometry by comparing the magnitudes derived for the same star in the long and short exposures. We found the match to be excellent, with any differences in magnitude being comparable to the photometric uncertainties in the short exposures (<0.03 mag).

The final combined catalog contains 22,291 stars with well-defined fluxes in the V and I bands. Of these, 18,142 objects are also detected in $H\alpha$. The CMD of all objects with combined photometric uncertainty in the V and I bands not exceeding 0.07 mag is shown in Figure 2.

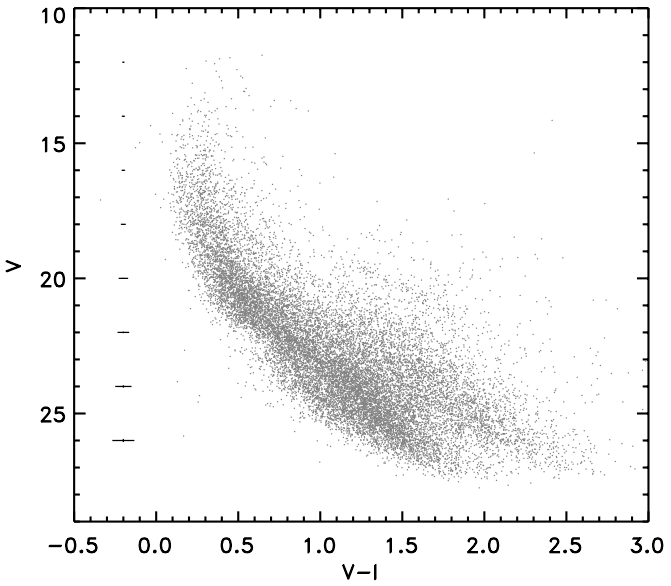

Figure 2. Color–magnitude diagram of the 30 Dor region covered by these observations in the V and I bands. Shown are all stars with a combined photometric uncertainty in V and I bands of less than 0.07 mag. The horizontal bars on the left-hand side of the figure indicate the typical uncertainty on the $V-I$ color as a function of magnitude.

4. DIFFERENTIAL REDDENING

The CMD shown in Figure 2 is the deepest so far obtained for this cluster. At $V - I \simeq 1.5$ it reaches about 3 mag deeper than the CMDs previously obtained with the WFPC2 camera on board the *HST* in these bands (Sirianni et al. 2000; Hunter et al. 1995a). Note that this is not only due to the improved sensitivity of the WFC3 camera, but also to the considerably shorter exposure times in the I band and the smaller field of view of the WFPC2 camera, which limited the observations to the most crowded regions of the cluster. The striking difference between the CMD shown in Figure 2 and that of Sirianni et al. (2000) is the prominent lower MS occupying the region fainter than $V \simeq 22$ and bluer than $V - I \simeq 1.5$ and revealing the presence in this field of a considerably older stellar population than the ∼3 Myr old stars associated with R 136 (e.g., De Marchi et al. 1993; Hunter et al. 1995a; Massey & Hunter 1998). We will discuss the age distribution of the stars in this field in Sections 5 and 6.

The other interesting feature seen in Figure 2 is the large number of objects in the range $0.5 \lesssim V - I \lesssim 2$ that appear brighter than the lower MS. Their location is consistent with that of the PMS population studied by Sirianni et al. (2000; see also Andersen et al. 2009), but their number is much larger than those detected before. We discuss the properties of these stars in Section 5, but we first need to address an important issue that affects the CMD, namely interstellar extinction.

The width of the upper MS seen in Figure 2, at $V \lesssim 20$, is much larger than the photometric uncertainty at those magnitudes (indicated by the horizontal bars on the left-hand side of the figure), revealing that there is a wide spread of extinction in this field. Actually, there is general consensus that differential reddening is present in these regions. From the analysis of high-resolution narrowband images, Hunter et al. (1995b) concluded that the nebulosity in this area is not uniform even on scales of order ∼10″. However, in a subsequent study of the stellar populations in this region, Hunter et al. (1996) opted for a uniform reddening correction across the whole field, since they concluded that uncertainties (e.g., red leak) in the response of the WFPC2 filters did not justify a star-by-star correction. Also, Sirianni et al. (2000) used the same A_V value for all stars, although this may have lead to larger uncertainties in their mass determination of individual PMS stars, as Selman et al. (1999) and more recently Andersen et al. (2009) have pointed out. In order to overcome this problem, in Section 4.1 we will use a robust method based on the determination of the individual reddening corrections for a large group of bright stars (Romaniello 1998), which are then used to derive a correction also for fainter neighboring objects.

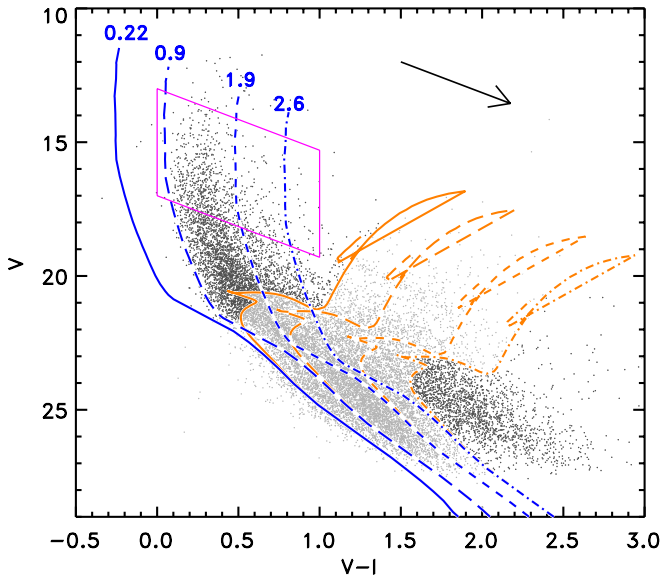

Figure 3. CMD of Figure 2 is compared here with theoretical isochrones from Marigo et al. (2008). The lines on the left-hand side of the figure (blue in the online journal) are for an age of 3 Myr, a metallicity of $Z = 0.007$, and a distance modulus of 18.6. Those on the right-hand side of the figure (orange in the online journal) are for the same distance and reddening, but for an age of 2 Gyr. The four line types correspond to different values of the extinction A_V, as indicated. Stars whose ages cannot be determined, even in an approximate way, from their position in the CMD are shown as light dots. The box indicates the stars in the upper MS that are used for reddening determination. Their slanted sides are parallel to the reddening vector indicated by the arrow (shown here for $A_V = 1.55$).

(A color version of this figure is available in the online journal.)

The young population in this field, responsible for the upper MS in Figure 2, has an age of ∼3 Myr (e.g., De Marchi et al. 1993; Hunter et al. 1995a) or perhaps younger (∼2 Myr) if Wolf–Rayet stars are still burning hydrogen (Massey & Hunter 1998; de Koter et al. 1998; Walborn et al. 1999). One can therefore determine the reddening toward each of those stars by measuring their color and magnitude displacements with respect to a theoretical isochrone for the appropriate age, metallicity, and distance. As for the metallicity, throughout this paper we will assume $Z = 0.007$ or about one-third $Z_\odot$, since this is a typical value for the LMC (e.g., Hill et al. 1995; Geha et al. 1998). As regards the distance to 30 Dor, we will use 51.4 ± 1.2 kpc since this is the geometrical distance to the neighboring SN 1987 object (Panagia et al. 1991, later updated in Panagia 1999). The resulting distance modulus of 18.6 is fully consistent with that adopted by Walborn & Blades (1997).

We show in Figure 3 as a solid line (in blue in the online version) an isochrone for an age of 3 Myr and a metallicity of $Z = 0.007$, from Marigo et al. (2008), and the adopted distance modulus of 18.6. Having assumed a younger age, i.e., 1 or 2 Myr, would have only affected the shape of the isochrone in the top ∼1 mag range, which we will not consider in this analysis. The isochrone is also already reddened by the amount corresponding to the intervening absorption along the line of sight due to the Milky Way, which Fitzpatrick & Savage (1984) quantified in $A_V = 0.22$, in turn corresponding to $E(V - I) = 0.1$.

The other curves on the left-hand side of the figure (in blue in the online version) represent the same isochrone reddened, for purpose of illustration, by an additional amount of extinction, with the long-dashed, short-dashed, and dot-dashed lines corresponding, respectively, to $A_V = 0.9$, 1.9, and 2.6. As for the extinction law, for the portion in addition to the $A_V = 0.22$ due to the Milky Way we have used the law determined spectroscopically by Scuderi et al. (1996) for Star 2 in the field of SN 1987A, which we take as representative of the 30 Dor region as well. The arrow in the figure shows the corresponding reddening vector for $A_V = 1.55$. The long-dashed line, corresponding to $A_V = 0.9$, forms a natural left envelope to the upper MS at $V < 20$ and leaves very few objects in the range $0.22 < A_V < 0.9$ at those magnitudes. This is expected because of the considerable amount of foreground extinction known to be present in the LMC toward 30 Dor: although the $\Delta A_V = 0.7$ value that we find is somewhat larger than the $\Delta A_V \simeq 0.5$ reported by Fitzpatrick (1985), the latter value has been determined for the brightest stars at the very center of 30 Dor that generally lie in evacuated cavities of H II gas of their own making and should therefore have a lower extinction. Note that, at magnitudes fainter than $V \simeq 22$, where the photometric uncertainty is still rather small (see bars in Figure 2), there is a large number of objects between the $A_V = 0.9$ and $A_V = 0.22$ curves. In fact, the latter offers a much better fit to the lower MS, suggesting that these stars belong to an older foreground population. At least some of them could be members of the much older LMC field, which is known to have ages in excess of ∼1 Gyr (e.g., Panagia et al. 2000; Harris & Zaritsky 2001).

Interestingly, there are also a few objects that appear bluer than the $A_V = 0.22$ curve. Although they are in general consistent with our photometric uncertainties, some of them could actually be very young stars with a circumstellar disk seen at high inclination (>85°). Objects of this type would appear somewhat bluer than their photospheric color due to light scattering on the circumstellar disk, as well as several magnitudes fainter than their photospheric brightness due to extinction along the line of sight caused by an almost edge-on disk. However, according to the models of Robitaille et al. (2006) for the spectral energy distribution of young stars seen at various viewing angles, objects of this type can only account for a few percent of the total young population, so the vast majority of stars near the $A_V = 0.22$ solid curve must belong to the field in the LMC foreground.

The presence of a foreground population of older objects becomes even more obvious when one looks at the other set of curves on the right-hand side of the figure (shown in orange in the online version), corresponding to isochrones for an age of 2 Gyr and the same metallicity, distance, and reddening values used for the 3 Myr isochrones, also from the models of Marigo et al. (2008). The 2 Gyr isochrones are shown up to a mass of $\sim 1.5\, M_\odot$, corresponding to the approximate location of the red giant clump (RC), a characteristic feature of the CMD of low-mass, metal-rich stars experiencing their He-burning phase. It represents the counterpart at high metallicity of the horizontal branch seen in CMDs of metal-poor globular clusters. The RC usually appears as a very tight, well-defined feature in the CMD of stellar populations that could in principle be used as a distance indicator (e.g., Stanek & Garnavich 1998; Paczynski & Stanek 1998; Cole 1998; Girardi et al. 1998; Girardi & Salaris 2001). When there is patchy absorption, like in our case, and the amount of extinction varies from place to place, the RC becomes in practice an elongated ellipse running parallel to the direction of the reddening vector. This is precisely the nature of the apparent sequence of points running diagonally between $1 < V - I < 2$ and $19 < V < 22$. This feature can also be used to derive the extinction law (De Marchi et al. 2007; Panagia et al. 2008).

The implications of this finding for the properties of the absorbing material in this and other LMC fields will be addressed in detail elsewhere (G. De Marchi & N. Panagia 2011, in preparation), but it is immediately clear from Figure 3 that the young and old stars present in this field have rather different extinction ranges. While stars in the RC span the entire range $0.22 \leqslant A_V \leqslant 2.6$, there are in practice no objects in the upper MS with $A_V < 0.9$. Therefore, the reddening correction that we can derive using the objects in the upper MS will only be valid for those stars and, in a statistical sense, for low-mass stars of similar age if they have a similar spatial distribution, but it will not be appropriate for older objects, for which we will have to resort to an average correction. The procedure that we followed for reddening correction is explained in detail in the following subsection.

4.1. Separate Extinction Correction for Younger and Older Stars

We have used all the upper MS objects inside the box shown in Figure 3 as reference stars for our determination of the reddening distribution across the field, with a total of about 800 stars selected in this way. Assuming that they are all MS stars, we have measured their displacement from the solid isochrone along the reddening vector, whose direction is given by the arrow and the tilted sides of the box (as mentioned above, we adopted the extinction law of Scuderi et al. 1996). We have explicitly excluded the brightest objects where an age difference of 1 or 2 Myr could have an effect, albeit small, on the shape of the isochrone. The reddening distribution ranges from $E(V-I) = 0.55$ or $A_V = 1.3$ to $E(V-I) = 0.9$ or $A_V = 2.1$, corresponding, respectively, to the 17% and 83% distribution limits, with a median value of $E(V-I) = 0.67$ or $A_V = 1.55$. The difference between the 17% and 83% limits gives a $\pm 1\sigma$ spread of 0.17 mag in $E(V-I)$, indicating that reddening varies considerably in this field.

The reddening values toward each of the selected MS stars were then used to derive a reddening correction for the objects in their vicinities. This procedure implicitly assumes that stars projected within a relatively small region of the field have similar extinction values, even though no information is available either on the depth of their distribution or on the uniformity of the absorbing material. In order to verify the validity of this assumption, we first applied the reddening correction to the upper MS stars themselves. Each star was corrected using the average of the extinction values of the nearest upper MS stars, excluding the star itself (no distance weighing was used, since we have no information on the depth of the distribution). After experimenting with a different number of neighbors (namely 1, 5, 10, and 20), we concluded that using the five closest neighbors produces the tightest upper MS. This choice corresponds to using reference stars within a radius of less than 10″, with a typical effective radius of ∼7.″5. After reddening correction, the $\pm 1\sigma$ spread in the upper MS drops to 0.10 mag and the upper MS itself appears considerably tighter in the CMD than in the raw data (see Figure 7). This result convinced us that the method, albeit statistical in nature, can be applied to other objects in the field, provided that they have an age and spatial distribution consistent with that of the upper MS stars.

The CMD and isochrones in Figure 3 help us to identify stars of similar age. This is the case for MS stars roughly brighter than $V = 20$ and bluer than $V - I = 1$ and for young PMS objects roughly redder and fainter than the dot-dashed 2 Gyr isochrone (these objects are shown as dark dots in the figure). However,

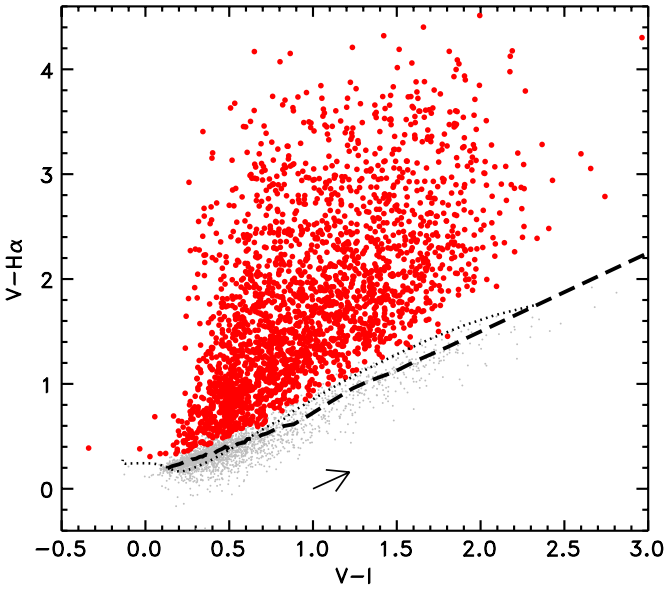

Figure 4. Color–color diagram used to identify stars with $H\alpha$ excess emission. Small dots represent all stars with combined photometric error in V, I, and $H\alpha$ of less than 0.05 mag. The dashed line represents the running median $V - H\alpha$ color, obtained with a box-car size of 100 points, whereas the thin dotted line shows the model atmospheres of Bessell et al. (1998) reddened by $A_V = 0.5$ mag according to the extinction law of Scuderi et al. (1996). The arrow in the figure corresponds to the reddening vector for $A_V = 0.5$ for the specific bands used in this study. A total of 2374 objects with a $V - H\alpha$ excess larger than 3σ are indicated with thick dots (in red in the online journal).

(A color version of this figure is available in the online journal.)

the CMD alone does not allow us to assign an age to objects falling in the region between the solid and dot-dashed 2 Gyr isochrones (shown as light dots), since they could be PMS stars of various ages, low-mass MS stars, or red giants. Therefore, in order to identify bona fide young objects in this region we have to resort to a more reliable youth indicator, namely a strong $H\alpha$ excess emission. This feature is characteristic of low-mass star formation and is attributed to the accretion process, whereby gravitational energy, released by infalling matter, ionizes and excites the surrounding gas (e.g., Königl 1991; Shu et al. 1994).

A detailed account on how to reliably detect these objects using multi-color photometry is given in De Marchi et al. (2010a) and De Marchi et al. (2011a). The method, already employed by Beccari et al. (2010) to search for objects with $H\alpha$ excess in NGC 3603, will be used in Section 5 for an accurate selection of bona fide PMS stars after reddening correction. Briefly, the method uses the median $V - H\alpha$ dereddened color of stars with small (<0.05 mag) photometric uncertainties in the three bands (V, I, and $H\alpha$) to define a reference template that is used to identify objects with excess $H\alpha$ emission. However, as De Marchi et al. (2010a) have shown, even before reddening correction the color–color diagram $V - H\alpha$, $V-I$ provides a robust identification of stars with $H\alpha$ excess, since in these bands the reddening vector runs almost parallel to the median photospheric colors of normal stars. Therefore, following that procedure, we looked initially for stars whose $V - H\alpha$ color exceeds by at least three times the photometric uncertainty the $V - H\alpha$ color of normal stars (i.e., those with no excess) with the same $V-I$ color. A more stringent selection will be applied after reddening correction (see Section 5).

The PMS candidates selected in this way, a total of 2374, are shown as thick dots in Figure 4, where the dashed line

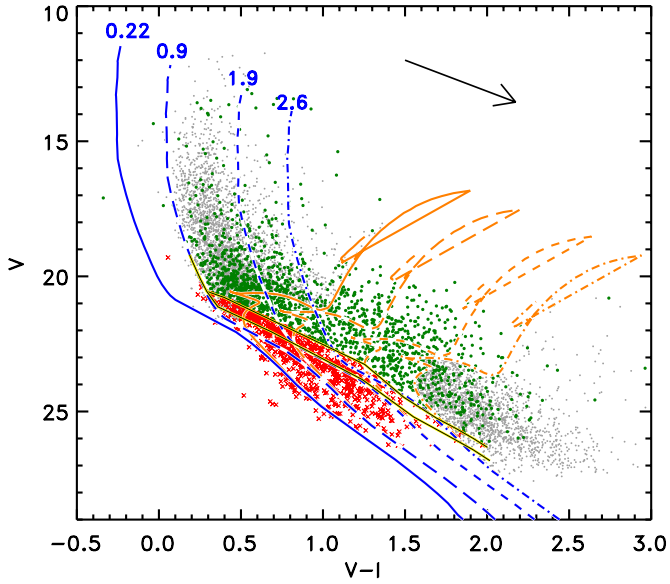

Figure 5. Same as Figure 3, but in addition we show the isochrones for PMS ages of 5 and 10 Myr (thin solid lines) for $A_V = 0.9$. Stars with $H\alpha$ excess emission located above and below the 5 Myr isochrone are indicated, respectively, with thick dots (green in the online journal) and crosses (red in the online journal) and are approximately younger and older than 5 Myr. The arrow corresponds to the reddening vector for $A_V = 1.55$, which is the median reddening value of upper MS stars.

(A color version of this figure is available in the online journal.)

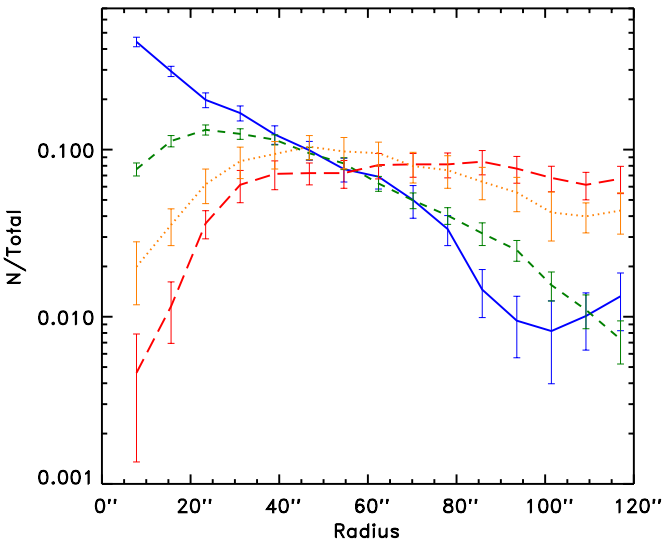

Figure 6. Radial distribution of upper MS stars (solid line), of low-mass stars with $H\alpha$ excess with ages younger than ∼5 Myr (short-dashed line) and older than ∼10 Myr (long-dashed line), as per Figure 5. The dotted line corresponds to stars with ages intermediate between 5 and 10 Myr. The curves are normalized by the number of objects in each sample (respectively, 812, 1637, 433, and 301), but the solid line is further rescaled by a factor of 0.6 for an easier comparison with the others. Error bars correspond to the Poisson uncertainty on the number counts.

(A color version of this figure is available in the online journal.)

represents the median photospheric $V - H\alpha$ color as a function of $V-I$. For comparison, we also show as a thin dotted line the corresponding colors derived from the model atmospheres of Bessell et al. (1998) for stars with effective temperatures in the range 3500 K $\leqslant T_{\rm eff} \leqslant$ 40,000 K, surface gravity $\log g = 4.5$, and a metallicity index [M/H] $= -0.5$, as appropriate for the LMC (Dufour 1984). The theoretical colors were calculated for the specific filters of the WFC3 camera and were reddened by $A_V = 0.5$, following the extinction law of Scuderi et al. (1996) mentioned above for the purpose of comparison with the data. Note that, due to the still preliminary calibration of the WFC3 photometric system in the $H\alpha$ band, we had to apply a small correction to the $V - H\alpha$ color of 0.05 mag to force the $V - H\alpha$ color of Vega to be 0 at $V - I = 0$, as is appropriate for the VEGAMAG photometric system.

The objects with $H\alpha$ excess emission are also shown as thick symbols in the CMD of Figure 5. Aside from the 3 Myr and 2 Gyr isochrones, we also show there the isochrones for PMS stars of ages 5 Myr (upper thin line) and 10 Myr (lower thin line) from the models of Degl'Innocenti et al. (2008) for the assumed LMC metallicity ($Z = 0.007$) and having taken $A_V = 0.9$ for the reddening.[26] These isochrones allow us to distinguish in an approximate way between younger and older PMS stars (a more accurate age determination requires the reddening correction and will be possible only at the end of this process) and to study their spatial distribution. Using the 5 Myr PMS isochrone as a reference, we have marked as thick dots and crosses, respectively, the objects above and below that line, and hence approximately younger and older than 5 Myr.

[26] Note that the ages of 5 and 10 Myr of these PMS isochrone are not counted from the zero-age main sequence (ZAMS) but from the birth line (see Palla & Stahler 1993 for a definition). For instance, the 5 Myr PMS isochrone meets the MS isochrone for age 3 Myr (counted from the ZAMS) at $V \simeq 21$, corresponding to $\sim$2.5 $M_\odot$. At this stage of PMS evolution, any more massive stars have already reached the MS.

In Figure 6 we show the radial distribution of these low-mass stars with $H\alpha$ excess, drawn from the nominal center of R 136. The short-dashed line corresponds to stars younger than ∼5 Myr, the long-dashed line to stars older than 10 Myr, while the distribution of upper MS stars is shown by the solid line, rescaled by a factor of 0.6 to make the comparison easier. Younger and older PMS stars have markedly different distributions: older stars have a rather uniform distribution and are almost absent inside a radius of ∼30″, while younger objects show a density gradient that follows remarkably well that of upper MS stars down to ∼10″, where photometric incompleteness starts to dominate as indicated by the rapidly increasing photometric uncertainties in these regions. The choice of which approximate age (5 Myr or 10 Myr) to adopt for separating "younger" and "older" stars is somewhat arbitrary, but the dotted line in Figure 6, corresponding to stars with ages in the range 5–10 Myr, suggests that objects with $H\alpha$ excess older than ∼5 Myr have a radial distribution remarkably different from that of upper MS stars. This is perhaps not surprising, considering that 5 Myr is about twice the age of the massive members of R 136 (2–3 Myr; De Marchi et al. 1993; Hunter et al. 1995a; Massey & Hunter 1998; de Koter et al. 1998; Walborn et al. 1999).

We will discuss these differences in the radial distribution in more detail in Section 6. For now, Figure 6 confirms that it is appropriate to use the reddening values derived from upper MS stars also for similarly young low-mass objects, but it suggests that this type of correction would not be suitable for older stars outside of the inner ∼50″. As Figure 6 implies, these objects are uniformly distributed over the field and are thus consistent with being in the foreground of R 136. In order to obtain at least an estimate of their reddening, we can use the stars with $H\alpha$ excess that appear bluer than the isochrone for $A_V = 0.9$, i.e., the long-dashed line in Figures 3 and 5.

As mentioned earlier, $A_V = 0.9$ is the lower limit to the reddening toward the upper MS stars of R 136, so objects bluer than the long-dashed line in those figures are most likely in

the foreground. A total of 144 stars satisfy this condition and, assuming that they are in the late stages of PMS evolution, i.e., close to the MS, we derive for them a median reddening value of $A_V = 0.5$. If these objects were in a considerably earlier stage of their PMS evolution, this procedure would give us an upper limit to their reddening. On the other hand, the fact that they are uniformly distributed over the field indicates that they cannot be as young as the other much more concentrated objects with $H\alpha$ excess (see Figure 6). We therefore take $A_V = 0.5$ as a representative value for the reddening toward all these stars and in general for all objects with $H\alpha$ excess shown as crosses in Figure 5.

We can now correct the magnitudes for extinction of all objects shown in Figure 5 in the following way. All stars located within 50″ of the center of R 136 are corrected individually using the average extinction value of the nearest five upper MS stars. As regards objects outside 50″, those with an age lower than ∼5 Myr (i.e., thick and thin dots in Figure 5) are corrected in the same way, whereas older stars with excess (crosses in Figure 5, red in the online journal) are corrected using the average $A_V = 0.5$ value. No correction is attempted for other objects, since we cannot determine their ages on the basis of the CMD alone, and they are not considered further in this work.

Note that when the magnitude of an object is corrected for extinction using its nearest neighbors, it is assumed that the placement of the object with respect to the absorbing material is similar to that of the reference stars in its vicinities. This process is accompanied by some statistical fluctuations, since as we have seen there is an intrinsic spread of 0.10 mag in the $E(V - I)$ distribution of our upper MS reference stars. However, the uncertainties that this assumption can introduce in the final magnitudes of the stars are relatively small. The typical standard deviation of the $E(V - I)$ values of the five nearest neighbors is 0.12 mag and, more generally, over the entire field these statistical uncertainties are not expected to exceed the reddening spread measured for the upper MS reference stars before reddening correction, i.e., 0.17 mag in $E(V - I)$ or ∼0.35 mag in A_V.

The CMD corrected for extinction in this way is shown in Figure 7. It must be understood that it does not cover all objects that were observed, but only those for which we could determine a reliable correction for reddening. The symbol types are the same as used in Figure 5; the solid line represents the theoretical isochrone from Marigo et al. (2008) for an MS age of 3 Myr, a metallicity of $Z = 0.007$, and a distance modulus of 18.6, whereas the dashed line corresponds to the isochrone of Degl'Innocenti et al. (2008) for a PMS age of 5 Myr and the same metallicity and distance modulus. The PMS isochrone of Degl'Innocenti et al. (2008) has been translated from the theoretical plane ($\log L$, $\log T_{\rm eff}$) to the plane of the observations using the model atmospheres of Bessell et al. (1998) folded through the specific WFC 3 filters employed here. The PMS isochrone meets the MS at $V_0 \simeq 19.5$ and it is reassuring that the two curves are in excellent agreement at brighter magnitudes, since they are based on independent models and different input physics.

5. PRE-MAIN-SEQUENCE STARS

The CMD corrected for extinction in Figure 7 reveals that at dereddened V_0 magnitudes fainter than 19 there is a conspicuous number of objects that are above (i.e., brighter than) the MS and, as such, they are consistent with a population of PMS stars. These objects extend down to $V_0 \simeq 26$ or more than

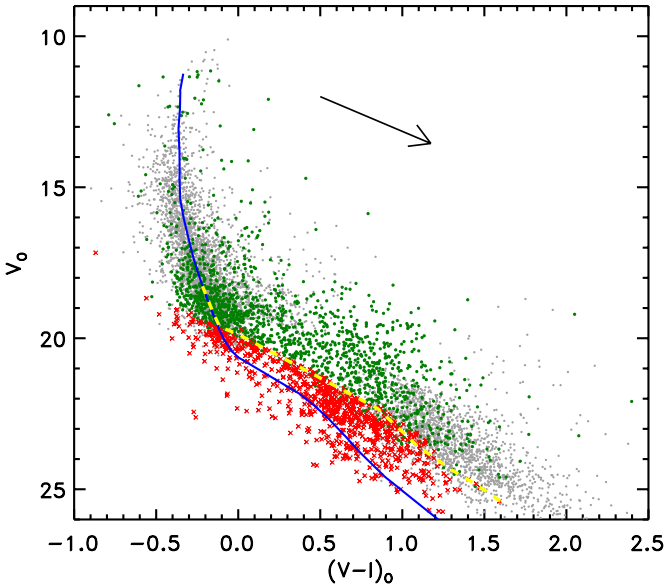

Figure 7. CMD corrected for reddening. Only stars for which a reddening correction could be derived are shown. The symbol types are the same as used in Figure 5 and so is the arrow, for $A_V = 1.55$. The solid line represents the theoretical isochrones from Marigo et al. (2008) for an MS age of 3 Myr, a metallicity of $Z = 0.007$, and a distance modulus of 18.6, while the dashed line corresponds to the isochrone of Degl'Innocenti et al. (2008) for a PMS age of 5 Myr and the same metallicity and distance modulus.

(A color version of this figure is available in the online journal.)

three magnitudes deeper than the limit reached by Sirianni et al. (2000) and Andersen et al. (2009), who detected and studied the brightest members of this population.

As already mentioned in Section 4, having corrected the photometry for extinction allows us to better clarify and confirm the PMS nature of these stars by looking at the specific signatures of the mass accretion process that is supposed to accompany this evolutionary phase. The accretion process is believed to be the cause of the strong excess emission observed in these objects (e.g., Königl 1991; Shu et al. 1994). For example, the presence of a strong $H\alpha$ emission line (with equivalent width in excess of ∼10 Å) in young stellar objects is normally interpreted as the signature of ongoing accretion (e.g., Feigelson & Montmerle 1999; White & Basri 2003). Note that, although it is customary to use negative equivalent widths for emission lines, in this work we will use $W_{\rm eq}^{E}(H\alpha)$ to refer to the equivalent width of the $H\alpha$ emission line, defined as a positive quantity.

In Section 4 we used this method for a preliminary coarse identification of stars with $H\alpha$ excess emission, but here we employ very conservative criteria to refine the selection of bona fide PMS stars. In particular, we now limit the search only to stars with a combined photometric uncertainty in the V, I, and $H\alpha$ bands of less than 0.1 mag and fainter than $V_0 = 17$ (corresponding to $\sim 300\,L_\odot$) and we look for objects with dereddened $(V - H\alpha)_0$ color excess at least four times larger than the photometric uncertainty in those bands (equivalent to a 4σ detection limit).

In Section 4 we used as a reference template the median photospheric colors of stars with small photometric uncertainty, the majority of which are older MS stars and have no $H\alpha$ excess. This approach cannot be followed here since many of the objects for which we could compute a reddening correction have $H\alpha$ excess. As a reference template we use instead the theoretical photospheric colors derived from model atmospheres. As

Figure 4 shows, the models of Bessell et al. (1998) for surface gravity $\log g = 4.5$ and metallicity $[M/H] = -0.5$ are in excellent agreement with the observed colors. This was also shown to be the case for stars in the field of SN 1987A (De Marchi et al. 2010a) and in NGC 346 (De Marchi et al. 2011a).

Besides selecting stars with excess emission above the 4σ level, we also imposed constraints on the equivalent width of the $H\alpha$ emission, $W_{\rm eq}^{E}(H\alpha)$. Following the procedure outlined in De Marchi et al. (2010a) to derive $W_{\rm eq}^{E}(H\alpha)$ from the observed colors, we further restricted the selection to objects with $W_{\rm eq}^{E}(H\alpha) > 20$ Å in order to avoid contamination by stars with significant chromospheric activity. Furthermore, since at temperatures $T_{\rm eff} \gtrsim 10{,}000$ K or colors $(V-I)_0 \lesssim 0$ the sample could be contaminated by Be stars that are evolving off the MS, for those objects we set a more stringent condition, namely $W_{\rm eq}^{E}(H\alpha) > 50$ Å. In a survey of about 100 stars of type Be in the Galaxy (Cote & Waters 1987), only one star is found with $W_{\rm eq}^{E}(H\alpha) > 50$ Å and the largest majority have values in the range from 4 Å to 30 Å.

A total of 1159 objects satisfy these conservative detection conditions: we will take them hereafter as bona fide PMS stars. Obviously, less stringent limits would result in a larger number of PMS stars, albeit with lower significance, but it must be understood that, even without changing the selection criteria, the actual number of PMS stars in this field must be considerably larger. This is because our detection and classification relies on the presence of $H\alpha$ excess emission at the time of the observations, but very young populations are known to show large variations in their $H\alpha$ emission over hours or days (e.g., Fernandez et al. 1995; Smith et al. 1999; Alencar et al. 2001), with only about one-third of them at any given time being active $H\alpha$ emitters with $W_{\rm eq}^{E}(H\alpha) > 10$ Å (Panagia et al. 2000; De Marchi et al. 2010a, 2011a).

Therefore, the 1159 stars identified as bona fide PMS objects are those that were undergoing active mass accretion and therefore showed $H\alpha$ excess emission at the time of these observations. On the other hand, since the duty cycles of any two stars are completely independent of one another, the sample of bona fide PMS stars identified in this way is representative of the entire PMS population in this field. Hereafter, unless otherwise indicated, when talking about PMS stars we will refer exclusively to the 1159 bona fide PMS objects identified through their $H\alpha$ excess emission.

We show in Figure 8 their locations in the CMD (thick dots). The majority occupy the region above the MS where young PMS objects are expected, but there are many located at or near the MS, suggesting an older age. A similar situation has already been noted in other star-forming regions, namely the SN 1987A field in the LMC (De Marchi et al. 2010a), NGC 3603 in the Milky Way (Beccari et al. 2010), and NGC 346 in the Small Magellanic Cloud (De Marchi et al. 2011a).

The skeptical reader might be concerned that the $H\alpha$ excess emission of many of the objects near the MS could in reality be due to nebular contamination of the gas present in the field. However, as mentioned in Section 3, we specifically excluded from our photometry all objects for which the photometric aperture would be contaminated by gas filaments. If the filament completely fills both the core aperture used to measure the flux of the star and the surrounding background annulus, it will not alter the photometry of the star, since it will be equivalent to a uniform background. Obviously, if the background annulus does not properly sample the contamination, for instance because the filament only covers part of it, the emission present in the gas may be erroneously associated with the object (for an illustration of this effect, see Beccari et al. 2010). Precisely for this reason, as discussed in Section 3, we have removed from the initial star lists all objects in the vicinity of a filament. Therefore, we are confident that the $H\alpha$ excess emission of our bona fide PMS stars is an intrinsic feature of those objects and we must interpret their distribution across the CMD as a sign of an age spread.

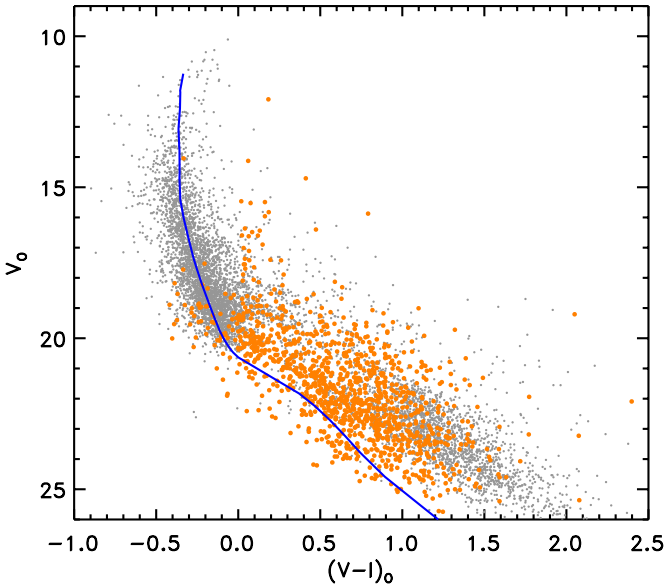

Figure 8. Thick dots mark bona fide PMS stars in the CMD corrected for extinction. The majority occupy the region above the MS where young PMS objects are expected, but there are several located at or near the MS, suggesting an older age. The solid line is the same as in Figure 7.

(A color version of this figure is available in the online journal.)

6. STAR FORMATION OVER TIME

More quantitative information on the age of these objects can be obtained from the comparison with PMS isochrones, shown in Figure 9, where the effective temperatures ($T_{\rm eff}$) and luminosities (L) of these stars are arranged in the H-R diagram. The value of $T_{\rm eff}$ was derived for each star directly from the dereddened $V-I$ color, since this is an excellent index for temperature determinations in the range 4000–10,000 K (e.g., von Braun et al. 1998; Bessell et al. 1998). For the conversion we made use of the models of Bessell et al. (1998) already discussed in Section 4. As for the bolometric luminosity, it was obtained from the dereddened V magnitude and the same models, having assumed a distance modulus of 18.6.

The solid lines in the figure corresponds to the PMS evolutionary track from the Pisa group (Degl'Innocenti et al. 2008; Tognelli et al. 2011) for metallicity $Z = 0.007$. The tracks correspond to stellar masses from $0.4\,M_{\odot}$ to $4.5\,M_{\odot}$ and reveal the presence of bona fide PMS stars over the entire mass range. The isochrones (dashed lines) correspond, from right to left, to ages ranging from 0.125 Myr to 32 Myr with a constant age step of a factor of two, selected in such a way that our photometric uncertainties are slightly smaller than the typical separation between the isochrones. PMS objects are seen across the entire age range.

6.1. Age Distribution of PMS Stars

The comparison of the H-R diagram with PMS evolutionary tracks and isochrones allows us to quantify the age spread of

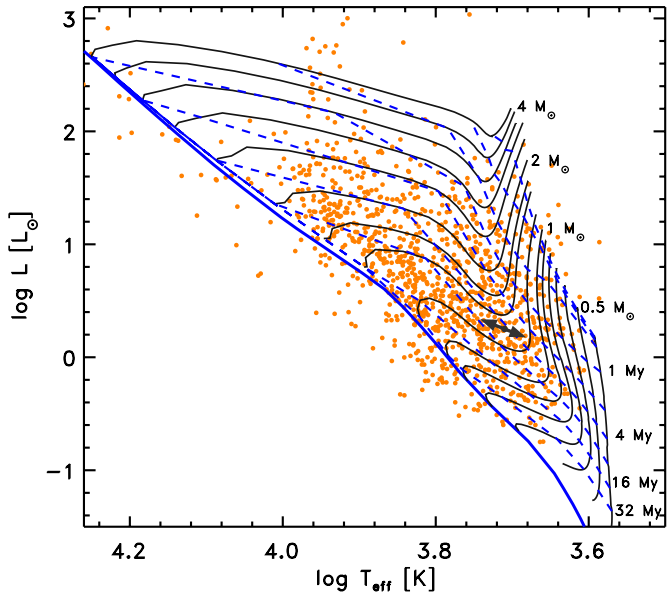

Figure 9. H-R diagram of the bona fide PMS stars. The solid lines correspond to the PMS evolutionary tracks of Degl'Innocenti et al. (2008) for $Z = 0.007$ and masses of 0.4, 0.5, 0.6, 0.7, 0.8, 0.9, 1.0, 1.2, 1.5, 1.7, 2.0, 2.5, 3.0, 3.5, 4.0, and 4.5 $M_{\odot}$, from bottom to top. The dashed lines indicate the PMS isochrones from the same models for ages or 0.125, 0.25, 0.5, 1, 2, 4, 8, 16, and 32 Myr, from right to left. The leftmost solid line represents the ZAMS of Marigo et al. (2008) for $Z = 0.007$ and, for $L > L_{\odot}$, it agrees rather well with the 32 Myr PMS isochrone. The good match between the two independent sets of models is also confirmed by the fact that the PMS evolutionary tracks end on the ZAMS. The double arrow at $\log T_{\rm eff} \simeq 3.7$ and $\log L \simeq 0.2$ indicates the effect of the $\pm 1\sigma$ reddening uncertainty of $\Delta E(V - I) = \pm 0.12$ mag.

(A color version of this figure is available in the online journal.)

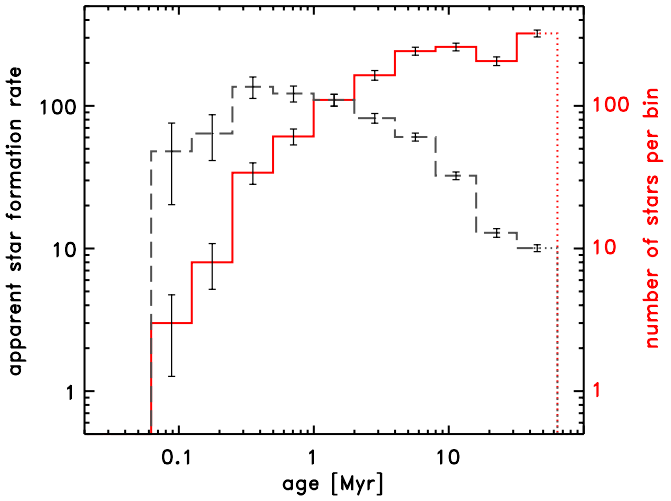

Figure 10. Histogram of the age distribution of PMS stars. Ages are binned using a constant logarithmic step (a factor of two). The solid line gives the number of stars inside each age bin, whereas the dashed line provides an apparent value of the star formation rate in units of stars per Myr.

(A color version of this figure is available in the online journal.)

the PMS stars that was already evident in the CMD. Individual stellar masses and ages were derived via interpolation over a finer grid than the one shown in the figure. We followed the interpolation procedure developed by Romaniello (1998), which does not make assumptions on the properties of the population, such as the functional form of the IMF. On the basis of the measurement errors, this procedure provides the probability distribution for each individual star to have a given value of the mass and age (the method is conceptually identical to the one presented recently by Da Rio et al. 2010).

An important aspect to consider is the uncertainty associated with the age determination of our PMS stars from their location in the H-R diagram. Besides photometric errors in the V- and I-band data (which are always less than 0.07 mag), the major sources of uncertainty are the effects of reddening and the comparison with stellar models. As regards the latter, De Marchi et al. (2010a) show that, excluding possible inaccuracies in the models' input physics and interpolation errors, the largest source of uncertainty comes from the use of models that do not properly describe the stellar population under study, e.g., because of the wrong metallicity and from differences between models of various authors. They conclude that systematic uncertainties of order 20% are to be expected for the mass and possibly higher for the age.

As for reddening, dust extinction systematically displaces stars in the H-R diagram toward lower luminosities and effective temperatures. Therefore, if the photometry of a PMS star is not corrected for reddening, its age will typically be underestimated. A study currently being conducted (G. De Marchi & N. Panagia, 2011, in preparation) shows that for reddening $E(V - I) < 1$ there is a rather linear relationship of the type $E(V - I) \simeq \log(t_r / t_0)$, where t_r and t_0 are the ages before and after reddening correction. For example, as discussed in Section 4, the spread of the upper MS in Figure 2 corresponds to a reddening spread of ± 0.17 mag in $E(V - I)$. Therefore, if we had used the average reddening value of $A_V = 1.55$ to correct the magnitudes of all young stars, instead of using the values of the nearest neighbors, we would have introduced an age uncertainty of a factor of $\sim$1.5. Similarly, if reddening correction for older stars with excess (i.e., those indicated by crosses in Figure 5) had been done using the average A_V value of the nearest upper MS neighbors instead of $A_V = 0.5$, the derived ages would be typically twice as old. As a further example, the double arrow in Figure 9 indicates the amount and direction of the displacement in the H-R diagram caused by the typical uncertainty of ± 0.12 mag in $E(V - I)$ associated with our reddening correction (see Section 4.1). In the specific case shown, the corresponding uncertainty on the age is a factor of $\sim$1.5 while the uncertainty on the mass is less than 15%.

This analysis suggests that the typical uncertainty on the ages that we derive is less than a factor of two. For this reason, the age distribution of PMS stars is shown in Figure 10 using as bin size a constant logarithmic step of a factor of two, which does not suffer from the relative age uncertainties. The solid line gives the number of stars inside each age bin as a function of time, whereas the dashed line provides an apparent value of the star formation rate in units of stars per Myr (i.e., the number of stars in each bin divided by the size of the bin).

The dashed line seems to suggest a rather uniform star formation rate over the past 4 Myr, of order $\sim$200 $M_{\odot}$ Myr^{-1} (the mass of our PMS stars younger than 4 Myr ranges from 1.1 $M_{\odot}$ to 3.2 $M_{\odot}$, respectively, the 17 and 83 percentiles, with an average of 2 $M_{\odot}$), and a progressive drop at earlier times. Obviously, this is necessarily a lower limit to the star formation rate, since our measurements only account for PMS stars in the range $\sim$0.5–4.0 $M_{\odot}$ that had $H\alpha$ excess emission at the time of the observations. Furthermore, since the fraction of PMS stars in an active state of accretion is expected to decrease with age (see De Marchi et al. 2011b), the apparent drop in the star formation beyond 2 Myr can at least in part be explained.

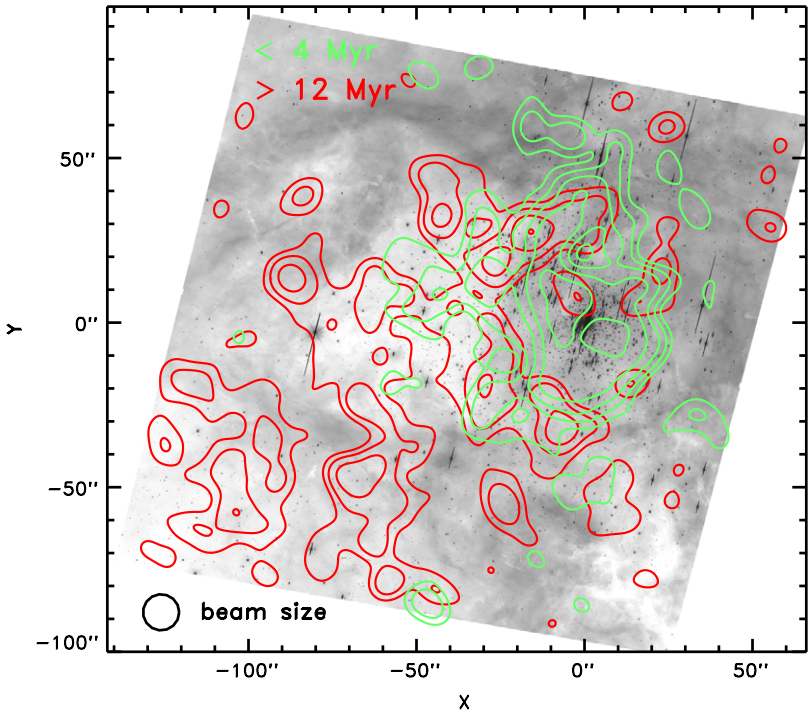

Figure 11. Contour lines showing the spatial density distribution of younger (<4 Myr; thin dark line on white thick line or green in the online journal) and older (>12 Myr; thick dark line or red in the online journal) PMS stars, overlaid on a negative $H\alpha$ image of the region. The (0, 0) position in this figure corresponds to the nominal center of R 136, with north pointing up and east to the left, like in Figure 1, but here we show the entire extent of the observed field. The contour plots have been obtained after Gaussian smoothing with a beam size of $\sigma = 4''$ or ∼1 pc, as indicated by the circle in the lower left corner. The step between contour levels is constant and corresponds to a factor of 1.5.

(A color version of this figure is available in the online journal.)

Keeping in mind that we can only provide a lower limit to the star formation rate, near the peak of the distribution, at ∼1 Myr, this limit corresponds to ∼330 $M_\odot$ Myr^{-1} (the average mass of those objects is 2.3 $M_\odot$), while at ∼16 Myr it drops by over an order of magnitude to ∼10 $M_\odot$ Myr^{-1} (average mass 1.3 $M_\odot$). A more detailed study of the star formation rate of 30 Dor will be the topic of a future paper, but the histograms in Figure 10 already show quite convincingly that star formation has been present in this region for an extended period of time, exceeding 30 Myr.

6.2. Spatial Distribution of PMS Stars

From a spectroscopic study of massive stars (>40 $M_\odot$) within a radius of ∼15′ of R 136, Selman et al. (1999) concluded that recent star formation in this region shows at least three distinct bursts, respectively, ∼5, ∼2.5, and ∼1.5 Myr ago, with increasing strength. They also found that the younger generation is considerably more concentrated than the others and is responsible for most of the star formation within 6 pc or ∼25″ of the cluster center. It is therefore useful to compare this picture with the spatial distribution of our PMS stars.

Although we do not have the age resolution needed to establish unambiguously whether the formation has been continuous during the past 30 Myr or whether repeated bursts have occurred, we can look at the current age distribution for clues as to the relationships between stars of different ages. The age distribution of these PMS stars is characterized by a median of ∼7 Myr, with about 35% of the stars being younger than ∼4 Myr and an equal number older than ∼12 Myr. Hereafter we will refer to these two groups, comprised of 415 objects each, as "younger" and "older" PMS stars, respectively. Note that, with a typical age uncertainty not exceeding a factor of two, these two groups are well separated in age, since the former has a median age of ∼2 Myr and the latter ∼18 Myr.

Interestingly, their projected spatial density distributions are also very different. They are shown in Figure 11 by contour lines of different colors, with logarithmic scaling, plotted over an image of the field in the $H\alpha$ band. The contour plots have been derived after smoothing the distribution with a Gaussian beam with size $\sigma = 4''$ or ∼1 pc, as indicated by the circle in the lower left corner of the figure. The lowest contour level corresponds to a local density of PMS stars twice as high as the average PMS star density over the entire field. The step between contour levels corresponds to a factor of 1.5.

There is a pronounced difference in the spatial distribution of younger and older PMS stars. The former are concentrated near the center of the R 136 cluster, where they form a density plateau, while older PMS stars preferentially occupy the region to the east of R 136 and are remarkably absent from the cluster center. Since these stars have a rather uniform distribution across the field, we should expect to find them also near the location of the young R 136 cluster, contrary to what we observe. Furthermore, with a median age of ∼18 Myr, these stars are considerably older than the ∼2 Myr old members of R 136, so we should not expect any spatial relationship (either a correlation or anti-correlation) between the distributions of the two types of objects, unless something else related to the younger population prevents us from detecting older PMS stars near the cluster center.

6.3. Erosion of Circumstellar Disks

Photometric incompleteness due to the young massive stars could seem an obvious culprit, since the younger PMS stars are on average brighter than the older objects. However, our analysis shows that the difference in the distribution of younger and older

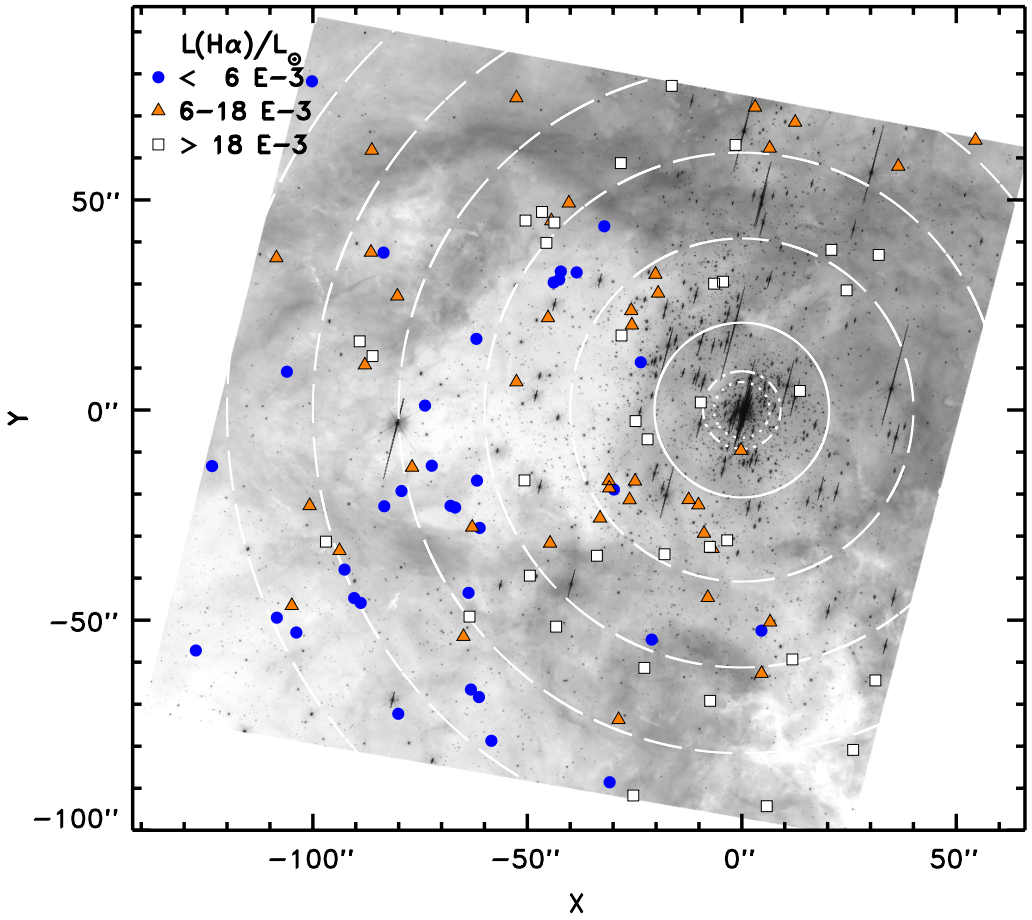

Figure 12. Spatial distribution of PMS stars with ages in the range 15–20 Myr. Different symbols are used, according to the $L(H\alpha)$ luminosity of these objects, as per the legend. Stars with lower $L(H\alpha)$ are systematically farther from the center of R 136.

(A color version of this figure is available in the online journal.)

PMS stars remains the same as shown in Figure 11 even when we restrict the choice of objects to the same magnitude range (e.g., $21 < V_0 < 23$). Therefore, the apparent paucity of older PMS stars near the center is not caused by selection effects in their detection.

A more likely explanation is the erosion of circumstellar disks via photo-evaporation caused by the far-ultraviolet radiation of the young massive members of R 136. If the disks of PMS stars are disrupted, the accretion process dwindles and these objects would no longer be detectable through their $H\alpha$ excess emission. To test this hypothesis, we have looked at how older PMS stars of various $H\alpha$ luminosity $L(H\alpha)$ are distributed in the field. In Figure 12 we show, as an example, all PMS stars with ages in the range 15–20 Myr (109 objects in total) using different symbols according to their $H\alpha$ luminosity. Dots correspond to stars with $L(H\alpha) < 6 \times 10^{-3}\ L_{\odot}$, squares to $L(H\alpha) > 1.8 \times 10^{-2}\ L_{\odot}$, and triangles to intermediate values. These values have been selected in such a way to have an equal number of objects in each group. In the background, we show as a reference a negative image of the field in the $H\alpha$ band.

The distribution of the three classes of objects is not random: stars with higher $L(H\alpha)$ are typically closer to the center of R 136 and located in areas where the background has a higher emission, whereas stars with lower $L(H\alpha)$ are farther away and preferentially in regions where the background emission is low. Although systematic differences in the mass of the three classes of objects could produce the observed distribution of $L(H\alpha)$, this can be excluded since the median mass of the three groups of stars is the same at $\sim$1.3 $M_{\odot}$. We can also exclude that this is an artifact of our photometry since the background is subtracted locally from each star (see Section 3) and therefore the diffuse $H\alpha$ nebular emission does not affect the intrinsic $H\alpha$ brightness of individual objects. However, a fraction of the $H\alpha$ luminosity of the stars closest to the center of R 136 could in principle be due to fluorescence of their circumstellar disks caused by the very strong ionizing radiation of the massive stars. It is, therefore, important to quantify this effect.

According to Massey & Hunter (1998), adopting the temperature calibration of Vacca et al. (1996), the total bolometric luminosity of the $\sim$30 brightest and most massive stars in R 136 is of order $4 \times 10^7\ L_{\odot}$ and most of them are of spectral type O4 or earlier. Based on this information and following Panagia (1973), we have determined at which distance from the center of R 136 the effects of the ionizing radiation impinging face-on on a circumstellar disk of radius 100 AU would contribute significantly to the $H\alpha$ luminosity of its star. The median $L(H\alpha)$ value of the PMS stars shown in Figure 12 is $0.01\ L_{\odot}$, so we have considered three cases of contamination, at approximately the 10%, 50%, and 100% level. The dotted, dot-dashed, and solid circles shown in Figure 12 correspond, respectively, to the distances at which the contribution to the $H\alpha$ luminosity due to fluorescence is $0.01, 0.005,$ and $0.001\ L_{\odot}$ (note that these distances are necessarily upper limits since they are projected on the plane of the sky and we have no information on the distribution of these objects along the line of sight). It is immediately

clear that the effects of fluorescence can only be important for a handful of stars, leaving the largest majority of old PMS objects in this field unaffected. The origin of the apparent correlation between their positions and $H\alpha$ luminosities has, therefore, to be found elsewhere.

A natural explanation would be that stars in regions of low emission, where the density of the gas is lower, such as those to the east of R 136, are much less shielded from the radiation of massive stars than objects in denser regions, such as those to the north and west of R 136. Therefore, their disks have been exposed to photo-evaporation for a longer time and their $H\alpha$ luminosity is today further reduced.

In support of this hypothesis, the photometry of all stars enclosed in the low-background region resembling a "Christmas tree" and centered at $(-50'', 20'')$, which is better seen in Figure 1, is consistent with a very low extinction value, close to the $A_V = 0.22$ indicated by Fitzpatrick & Savage (1984) as the contribution of the Milky Way to the intervening absorption along the line of sight. Furthermore, this region is characterized by very low emission at IR (e.g., Indebetouw et al. 2009) and radio wavelengths (e.g., Johansson et al. 1998; Rubio et al. 1998), confirming that it is devoid of both dust and gas. The region also corresponds with a high-velocity structure seen by Chu & Kennicutt (1994) in their detailed $H\alpha$ echelle study of the kinematics of 30 Dor. These authors find a bright redshifted knot 75″ east of R 136, with a velocity offset of ∼130–140 km s^{-1} and very low emission. The knot is part of a fast expanding shell to the east of the cluster that correlates well with a region of diffuse X-ray emission seen in images obtained with the *Einstein* satellite. These authors conclude that both the high-velocity features and the X-ray emission are related to high-velocity shocks from fast stellar winds and supernovae.

This picture is supported by the later study of 30 Dor by Townsley et al. (2006) with the *Chandra X-ray Observatory*. Their observations reveal rather strong diffuse emission in the area of the "Christmas tree" (their region 6, coincident with the east fast shell of Chu & Kennicutt 1994) with an absorption-corrected X-ray surface brightness of $\sim 6 \times 10^{32}$ erg s^{-1} pc^{-2} in the 0.3–2.2 keV band. A spectral fit to this emission shows a soft thermal plasma with $k\,T = 0.4$ keV (Townsley et al. 2006). Therefore, in such an evacuated region, the disks of PMS stars must be much more exposed to photo-evaporation.

Conversely, as discussed in Section 4, extinction toward the young massive stars at the center of R 136 is both higher and highly variable, indicating a much denser environment where gas and dust can intercept a significant fraction of the UV radiation from the massive central stars, thereby reducing the efficiency of the photo-evaporation process. Indeed, most of the PMS stars with $L(H\alpha) > 0.025\,L_\odot$ in Figure 12 are in regions of significant ^{12}CO(1 − 0) emission, suggesting a high density of molecular gas, and the column density in H I in front of R 136 is known to be very high ($\log N = 21.80 \pm 0.15$ cm^{-2}; de Boer et al. 1980).

Thus, although this picture is still necessarily qualitative, it provides a plausible explanation of the observed distribution of $H\alpha$ luminosities of older PMS stars across the field via the effects of photo-evaporation. These effects have been discussed by De Marchi et al. (2010a) in the field of SN 1987A. In that environment, located ∼20′ or 300 pc southwest of 30 Dor, the PMS stars around the hottest massive young stars are both less numerous and fainter in $H\alpha$ emission, suggesting that their circumstellar disks have been eroded more efficiently by enhanced photo-evaporation.

Unlike the relatively simple case of the SN 1987A field where little gas is present, the interstellar medium in 30 Dor is known to be much denser and highly fragmented, with considerable density variations across the field (e.g., Poglitsch et al. 1995). From the $H\alpha$ echelle study mentioned above, Chu & Kennicutt (1994) conclude that the kinematics of 30 Dor is dominated by a large number of expanding structures, over scales of 2–20 pc and with expansion velocities of 100–300 km s^{-1} and kinetic energies of 0.5–10 × 10^{50} erg. These structures are probably associated with supernova remnants embedded in supershells produced by stellar winds and supernovae explosions.

These processes can release a large amount of kinetic energy into the surrounding environment, and as such they could in principle contribute to the dissipation of circumstellar disks, adding to the effects of photo-evaporation. To better understand this, it is useful to calculate the amount of kinetic energy possibly deposited on such a disk by a nearby supernova explosion. We will assume hereafter a total energy release of $E = 1$ foe = 10^{51} erg per supernova explosion, a circumstellar radius $r = 100$ AU around a PMS star located at a distance of $d = 10$ pc from the supernova. The maximum fraction of energy deposited on such a disk hit face-on by the blast can be written as $\eta_E = E\,\pi\,r^2/d^2$ and amounts to $\sim 7.4 \times 10^{42}$ erg for the specific parameters assumed here. The motion that this energy release can impart onto the material of the disk depends on the total mass and size of the disk and hence on its density, which in turn could depend, e.g., on the radial location. In the simplified case of a homogeneous disk of mass m_d that we express as a fraction ϕ of the total stellar mass m, i.e., $m_d = \phi\,m$, the velocity v imparted by the ejecta to the disk material can be expressed as

$$v = 0.86 \times \left[\frac{d}{10\,\mathrm{pc}}\right]^{-1} \left[\frac{r}{100\,\mathrm{AU}}\right] \left[\phi\,\frac{m}{M_\odot}\right]^{-1/2} \mathrm{km\,s^{-1}} \quad (1)$$

De Marchi et al. (2011a) have shown that stars in the Magellanic Clouds accrete a substantial fraction of their total mass during the PMS phase, particularly at low masses, so for an order-of-magnitude calculation it is not unreasonable to assume $\phi = 1/2$.

We can see in this way that for a star with $m = 1\,M_\odot$ at a distance of 10 pc, the supernova ejecta hitting the disk face-on would impart a motion to its material with a velocity of ∼1 km s^{-1}. This value is about a factor of five smaller than the escape velocity at the edge of the disk for the typical PMS stars that we detect in the "Christmas tree" (median mass $\sim 1.3\,M_\odot$). For a disk seen under a smaller solid angle, the effect would be proportionally smaller. Less massive disks around less massive stars located closer to the supernova would obviously experience a much stronger effect. For instance, for a star of mass $1/4\,M_\odot$ at a distance of 1 pc from the supernova, the impulse received by the disk material would be sufficient to exceed the escape velocity at $r \gtrsim 1$ AU. This could significantly affect or possibly even stop the accretion process, eventually limiting the final mass of the star. On the other hand, with an average surface density of ∼0.7 PMS stars per pc^2, only a very small fraction of the disks around objects in this field would be severely affected by any one supernova explosion.

In summary, it is clear that the interplay between shocks and photo-evaporation effects due to the massive members of R 136 can have important consequences on disk erosion, potentially affecting the formation of low-mass stars in these regions. However, without more specific kinematical information for individual objects, it remains difficult to quantify the expected effects on the circumstellar disks of PMS stars using photometry

alone. For a better understanding of this complex region and a more quantitative characterization of the differences between the regions preferentially occupied by older PMS stars with high and low $L(H\alpha)$, we may have to await high spectral and spatial resolution spectroscopic observations to obtain a map of the amount and kinematics of the gas in the interstellar medium along the lines of sight toward these objects.

6.4. Causal Effects

Finally, we briefly address the implications of our findings for the current understanding of whether and how different generations of stars in 30 Dor are causally connected. Walborn & Blades (1987) and Walborn (1991) reported three early O stars embedded in dense nebular knots to the north and west of R 136 and suggested that these objects could belong to a younger generation, triggered by the energy released by R 136. Using ground-based spectral classification of a large number of OB stars in the 30 Dor nebula, Walborn & Blades (1997) studied the ages and spatial distribution of these objects, discovering an additional eight early O stars embedded in dense nebular knots. From a morphological analysis of these regions, they concluded that 30 Dor has a two-stage starburst structure in which the energetic activity of the 2–3 Myr old R 136 has triggered the formation of a younger (<1 Myr) generation of stars at a typical projected distance of ∼15 pc, inside the dense molecular clouds that surround R 136 to the northeast and west. Later IR observations with NICMOS (Walborn et al. 1999; Brandner et al. 2001) resolved many of these knots into many new IR sources, including multiple systems, clusters, and nebular structures, indicating active star formation.

From mainly morphological considerations in this and other Galactic star-forming regions, Walborn et al. (1999; see also Walborn 2002) suggested that this mode of two-stage starburst, with generations separated by ∼2 Myr, is ubiquitous. They concluded that in 30 Dor the first generation of stars, still present, is now triggering the birth of the second, peripheral generation of very massive stars, which in a few million years will be the only one left, after the most massive stars in the core of R 136 have disappeared. These authors predict 30 Dor to become a giant shell H II region like N11 and NGC 604, with its most massive stars around the periphery.

Our discovery of a considerable spread in the ages of PMS stars in this region, with the younger generation confined to the cluster's center and older objects uniformly distributed across the field (see Figure 11), raises some questions as to the validity of this picture at least as regards the formation of low-mass stars triggered by older (massive) objects in their vicinities. For instance, if we compare the projected distribution of PMS stars with ages of less than 2 Myr with that of objects in the age range 4–8 Myr we see that they have the same center, with the former slightly more concentrated, rather than distributed in the periphery of the latter as suggested in Walborn's (2002) triggered massive star formation scenario. As already shown in Figure 11, the stars around the periphery of R 136 are systematically older and not younger than the members of R 136 itself. The same conclusion had been reached by Selman et al. (1999) from a spectroscopic study of the massive stars ($>40\,M_{\odot}$) in these regions. Our findings suggest that if causal effects are present between different generations of stars, their interpretation cannot rely only on the relative ages and projected distributions of the objects, but must consider proper kinematical and possibly dynamical information. While it is undeniable that we are seeing a case of sequential star formation, in the sense that there are separate generations of stars over time, no clear signs of causal effects are seen. Therefore, although the concept of triggered star formation may well be valid, its relevance in the case of 30 Dor has yet to be demonstrated.

7. SUMMARY AND CONCLUSIONS

We have studied the properties of the stellar populations in the central regions of the 30 Dor cluster in the LMC using observations obtained with the WFC3 camera on board the *HST* in the V, I, and $H\alpha$ bands. The main results of this work can be summarized as follows.

1. Our photometry delivers the deepest CMD so far obtained for this cluster, reaching down to $V \simeq 27$ or about 3 mag deeper than previous *HST* observations, and reveals for the first time a prominent lower MS fainter than $V \simeq 22$. We attribute this feature to a stellar population considerably older than the ∼3 Myr old stars associated with R 136. The CMD shows also a large number of objects in the range $0.5 \lesssim V - I \lesssim 2$ that appear brighter than the lower MS and that are consistent with, but extend much deeper than, the population of PMS stars detected and studied by Sirianni et al. (2000) and Andersen et al. (2009).
2. The observations also reveal the presence of considerable differential extinction across the field. We quantify the total extinction toward massive MS stars younger than ∼3 Myr to be in the range $1.3 < A_V < 2.1$ (respectively, the 17% and 83% levels) with a median value of $A_V = 1.55$. We show that these stars can be used to derive a statistical reddening correction also for stars in their vicinities, if they have a similar age and spatial distribution. However, this is not the case for older stars, which show a broader reddening distribution starting already at $A_V = 0.22$ (corresponding to the contribution of the Milky Way along the line of sight toward 30 Dor). A proper correction for extinction, therefore, requires at least an approximate knowledge of the age of the stars, which is not possible for all objects in the CMD.
3. In order to distinguish relatively young objects from older stars, we looked for stars with $H\alpha$ excess emission, since this feature identifies candidate PMS stars, and we studied their distribution both across the field and in the CMD. Younger PMS stars follow the spatial distribution of massive stars and this allows us to correct them for reddening individually, using the extinction information derived for the massive objects. On the other hand, older PMS objects are uniformly distributed over the field and appear to be systematically less reddened than younger PMS stars. We derive for them an average extinction correction of $A_V = 0.5$.
4. Reddening correction allows us to proceed to a more accurate identification of bona fide PMS stars. We searched for stars with $V - H\alpha$ color exceeding that of normal stars at the 4σ level or more and with $W_{\rm eq}^{E} > 20$ Å (or >50 Å for stars with $T_{\rm eff} > 10{,}000$ K), in order to avoid contamination by stars with chromospheric activity or by the winds of Be stars. A total of 1159 objects satisfy these stringent conditions and we take them as bona fide PMS stars.
5. We derived the age of PMS stars through the comparison with theoretical PMS isochrones for metallicity $Z = 0.007$, as appropriate for the LMC. About 1/3 of these objects are younger than 4 Myr and an equal number are older than 12 Myr, indicating that star formation in this field has

proceeded over a long time, although our age resolution does not allow us to discriminate between an extended episode and a series of short and frequent bursts. As regards the past 4 Myr, we obtain a lower limit to the star formation rate of $\sim$200 $M_{\odot}$ Myr^{-1} for objects in the range $\sim$0.5–4 $M_{\odot}$.

6. We find a pronounced difference in the spatial distribution of younger (<4 Myr) and older (>12 Myr) PMS stars. The former are concentrated near the center of R 136, whereas older PMS objects are mostly located to the east of it and are remarkably absent near the cluster center. This effect, which is not due to photometric incompleteness, is in general consistent with the photo-evaporation of the circumstellar disks of older stars caused by the UV radiation of the massive members of R 136. However, not all older PMS stars are affected in the same way, since some are in regions where the high density of the molecular gas can reduce the efficiency of the photo-evaporation process.
7. Our results show that several generations of stars are present in this field, since there are objects with ages ranging from less than 1 to over 30 Myr, although no clear signs of causal effects or of triggered star formation are seen. It appears, however, that the presence of the massive R 136 cluster is sculpting the region and affecting low-mass neighboring objects through the effects of photo-evaporation.

We are grateful to an anonymous referee, whose suggestions have helped us to improve the presentation of this work. This paper is based on Early Release Science observations made by the WFC3 Scientific Oversight Committee. We are grateful to the Director of the Space Telescope Science Institute for awarding Director's Discretionary time for this programme. F.P. is grateful to the Space Science Department of ESA for their hospitality via the visitor programme. N.P. acknowledges partial support by *HST*-NASA grants GO-11547.06A and GO-11653.12A, and STScI-DDRF grant D0001.82435.

REFERENCES

Alencar, S., Johns-Krull, C., & Basri, G. 2001, AJ, 122, 3335
Andersen, M., Zinnecker, H., Moneti, A., McCaughrean, M., Brandl, B., Brandner, W., Meylan, G., & Hunter, D. 2009, ApJ, 707, 1347
Beccari, G., et al. 2010, ApJ, 720, 1108
Bessell, M., Castelli, F., & Plez, B. 1998, A&A, 333, 231
Brandl, B. 2005, in Starbursts: From 30 Doradus to Lyman Break Galaxies, ed. R. de Grijs & R. M. González Delgado (Astrophysics and Space Science Library, Vol. 329; Dordrecht: Springer), 49
Brandl, B., et al. 1996, ApJ, 466, 254
Brandner, W., Grebel, E., Barba, R., Walborn, N., & Moneti, A. 2001, AJ, 122, 858
Chu, Y.-H., & Kennicutt, R. 1994, ApJ, 425, 720
Cole, A. A. 1998, ApJ, 500, L137
Cote, J., & Waters, L. 1987, A&A, 176, 93
Da Rio, N., Gouliermis, D. A., & Gennaro, M. 2010, ApJ, 723, 166
de Boer, K., Koornneef, J., & Savage, B. 1980, ApJ, 236, 769
Degl'Innocenti, S., Prada Moroni, P. G., Marconi, M., & Ruoppo, A. 2008, Ap&SS, 316, 25
de Koter, A., Heap, S., & Hubeny, I. 1998, ApJ, 509, 879
De Marchi, G., Nota, A., Leitherer, C., Ragazzoni, R., & Barbieri, C. 1993, ApJ, 419, 658
De Marchi, G., Panagia, N., & Romaniello, M. 2007, in IAU Symp. 241, Stellar Populations as Building Blocks of Galaxies, ed. A. Vazdekis & R. Peletier (Cambridge: Cambridge Univ. Press), 333
De Marchi, G., Panagia, N., & Romaniello, M. 2010a, ApJ, 715, 1
De Marchi, G., Panagia, N., Romaniello, M., Sabbi, E., Sirianni, M., Prada Moroni, P., & Degl'Innocenti, S. 2011a, ApJ, in press (arXiv:1104.4494)
De Marchi, G., Panagia, N., & Sabbi, E. 2011b, ApJ, in press (arXiv:1106.5780)
De Marchi, G., Paresce, F., & Portegies Zwart, S. 2010b, ApJ, 718, 105
Dressel, L., et al. 2010, Wide Field Camera 3 Instrument Handbook, Version 2.1 (Baltimore, MD: STScI)
Dufour, R. 1984, in IAU Symp. 108, Structure and Evolution of the Magellanic Clouds, ed. S. van den Bergh & A. de Koter (Dordrecht: Reidel), 353
Feigelson, E., & Montmerle, T. 1999, ARA&A, 37, 363
Fernandez, M., Ortiz, E., Eiroa, C., & Miranda, L. 1995, A&AS, 114, 439
Fitzpatrick, E. 1985, ApJ, 299, 219
Fitzpatrick, E., & Savage, B. 1984, ApJ, 279, 578
Geha, M., et al. 1998, AJ, 115, 1045
Girardi, L., Groenewegen, M., Weiss, A., & Salaris, M. 1998, MNRAS, 301, 149
Girardi, L., & Salaris, M. 2001, MNRAS, 323, 109
Harris, J., & Zaritsky, D. 2001, ApJS, 136, 25
Hill, V., Andrievsky, S., & Spite, M. 1995, A&A, 293, 347
Hunter, D., O'Neil, E., Lynds, R., Shaya, E., Groth, E., & Holtzman, J. 1996, ApJ, 459, L27
Hunter, D., Shaya, E., Holtzman, J., Light, R., O'Neil, E., & Lynds, R. 1995a, ApJ, 448, 179
Hunter, D., Shaya, E., Scowen, P., Hester, J., Groth, E., Lynds, R., & O'Neil, E. 1995b, ApJ, 444, 758
Indebetouw, R., et al. 2009, ApJ, 694, 84
Johansson, L., et al. 1998, A&A, 331, 857
Kalirai, J., et al. 2009, WFC3 SMOV Proposal 11450: The Photometric Performance and Calibration of WFC3/UVIS, Instrument Science Report WFC3 2009–31 (Baltimore, MD: STScI)
Königl, A. 1991, ApJ, 370, L39
Malin, D. 1977, AAS Photo Bull., 16, 10
Marigo, P., Girardi, L., Bressan, A., Groenewegen, M., Silva, L., & Granato, G. 2008, A&A, 482, 883
Massey, P., & Hunter, D. 1998, ApJ, 493, 180
Paczynski, B., & Stanek, K. 1998, ApJ, 494, L219
Palla, F., & Stahler, S. 1993, ApJ, 418, 414
Panagia, N. 1973, AJ, 78, 929
Panagia, N. 1999, in IAU Symp. 190, New Views of the Magellanic Clouds, ed. Y.-H. Chu, N. Suntzeff, J. Hesser, & D. Bohlender (Cambridge: Cambridge Univ. Press), 549
Panagia, N., De Marchi, G., & Romaniello, M. 2008, in ASP Conf. Ser. 388, Mass Loss from Stars and the Evolution of Stellar Clusters, ed. A. de Koter, L. Smith, & L. Waters (San Francisco, CA: ASP), 413
Panagia, N., Gilmozzi, R., Macchetto, F., Adorf, H.-M., & Kirshner, R. P. 1991, ApJ, 380, L23
Panagia, N., Romaniello, M., Scuderi, S., & Kirshner, R. 2000, ApJ, 539, 197
Poglitsch, A., Krabbe, A., Madden, S., Nikola, T., Geis, N., Johansson, L., Stacey, G., & Sternberg, A. 1995, ApJ, 454, 293
Robitaille, T., Whitney, B., Indebetouw, R., Wood, K., & Denzmore, P. 2006, ApJS, 167, 256
Romaniello, M. 1998, PhD thesis, Scuola Normale Superiore, Pisa, Italy
Rubio, M., Barba, R., Walborn, N., Probst, R., Garcia, J., & Roth, M. 1998, AJ, 116, 1708
Scuderi, S., Panagia, N., Gilmozzi, R., Challis, P., & Kirshner, R. 1996, ApJ, 465, 956
Selman, F., Melnick, J., Bosch, G., & Terlevich, R. 1999, A&A, 347, 532
Shu, F., Najita, J., Ruden, S., & Lizano, S. 1994, ApJ, 429, 727
Sirianni, M., Nota, A., Leitherer, C., De Marchi, G., & Clampin, M. 2000, ApJ, 533, 203
Smith, K., Lewis, G., Bonnell, I., Bunclark, P., & Emerson, J. 1999, MNRAS, 304, 367
Stanek, K., & Garnavich, P. 1998, ApJ, 503, L131
Tognelli, E., Prada Moroni, P., & Degl'Innocenti, S. 2011, A&A, in press (arXiv:1107.2318)
Townsley, L., Broos, P., Feigelson, E., Brandl, B., Chu, Y.-H., Garmire, G., & Pavlov, G. 2006, AJ, 131, 2140
Vacca, W., Garmany, C., & Shull, J. 1996, ApJ, 460, 914
von Braun, K., Chiboucas, K., Minske, J. K., Salgado, J., & Worthey, G. 1998, PASP, 110, 810
Walborn, N. 1991, in IAU Symp. 148, The Magellanic Clouds, ed. R. Haynes & D. Milne (Dordrecht: Kluwer), 145
Walborn, N. 2002, in ASP Conf. Ser. 267, Hot Star Workshop III: The Earliest Stages of Massive Star Birth, ed. P. Crowther (San Francisco, CA: ASP), 111
Walborn, N., Barba, R., Brandner, W., Rubio, M., Grebel, E., & Probst, R. 1999, AJ, 117, 225
Walborn, N., & Blades, J. 1987, ApJ, 323, L65
Walborn, N., & Blades, J. 1997, ApJS, 112, 457
Weigelt, G., et al. 1991, ApJ, 378, L21
White, R., & Basri, G. 2003, ApJ, 582, 1109
Zinnecker, H., et al. 2002, in IAU Symp. 207, Extragalactic Star Clusters, ed. D. Geisler, E. Grebel, & D. Minniti (San Francisco, CA: ASP), 531